Optimized electrostatic inchworm motors using a flexible driving arm

2013 J. Micromech. Microeng. 23 015018

(http://iopscience.iop.org/0960-1317/23/1/015018)

J. Micromech. Microeng. **23** (2013) 015018 (12pp) doi:10.1088/0960-1317/23/1/015018

Optimized electrostatic inchworm motors using a flexible driving arm

I Penskiy and S Bergbreiter

Department of Mechanical Engineering and Institute for Systems Research, University of Maryland, 2181 Glenn L. Martin Hall, College Park, MD 20742, USA

E-mail: sarahb@umd.edu

Received 27 August 2012, in final form 6 November 2012
Published 13 December 2012
Online at stacks.iop.org/JMM/23/015018

Abstract

A new motor architecture that uses in-plane electrostatic gap-closing actuators along with a flexible driving arm mechanism to improve motor force density is introduced, optimized, manufactured, and tested. This motor operates similarly to other inchworm-based microactuators by accumulating small displacements from the actuators into much larger displacements in the motor. Using an analytical model of the inchworm motor based on the static force equilibrium condition, optimizations of a full motor design were performed to maximize motor force density. In addition, force losses from supporting flexures were included to calculate the theoretical motor efficiency for different motor designs. This force density optimization analysis of the gap-closing actuators and supporting motor structures provided the basis for designing and manufacturing inchworm motors with flexible driving arms and gap-closing actuators. The motor required only a single-mask fabrication and demonstrated robust performance, a maximum speed of 4.8 mm s^{-1}, and a maximum force on the shuttle of 1.88 mN at 110 V which corresponds to area force density of 1.38 mN mm^{-2}. In addition, instead of estimating motor force based on drawn or measured dimensions which often overestimates force, the demonstrated maximum motor force was measured using calibrated springs. The efficiency of the manufactured motor was measured at 8.75% using capacitance measurements and useful work output.

(Some figures may appear in colour only in the online journal)

1. Introduction

High force density linear microactuators (defined by a volume less than 1 mm^3) are of scarce availability but in great demand for numerous research and commercial endeavors including microrobotics [1], micropositioning [2], microassembly [3], and other applications. Actuator metrics of interest for many of these applications are high stall force, force density, and bandwidth. A less quantifiable metric for the microactuators is how easily they can be assembled into larger systems; it is much more difficult to assemble a separately fabricated actuator with a mechanism that it drives, than to manufacture both of these parts together as a monolithic device. The most successful examples of microrobots prove this point. Ebefors [4] used an assembly-free process in the design of a walking microrobot with thermal actuators, and Sreetharan designed a new process for manufacturing the flapping wing Robobee that included the piezoelectric actuators for driving the wing mechanisms [5]. Assembly-free processes also increase repeatability and reliability of the manufactured components. For these reasons, this paper will target a single mask microfabrication process in which actuators can be fabricated along with mechanisms in a variety of microfabrication processes.

Several actuation methods are available using microfabrication. The most common are piezoelectric, electrothermal, and electrostatic. Each actuation method has its benefits and drawbacks. Piezoelectric actuators have high force densities and high speed/bandwidth [1], but their manufacturing is more complex which makes their use less favorable for an assembly-free process. Electrothermal actuators produce very high forces and can be manufactured using standard microfabrication processes, but their power consumption and inefficiency make them a poor choice for systems like microrobotics that require high actuation

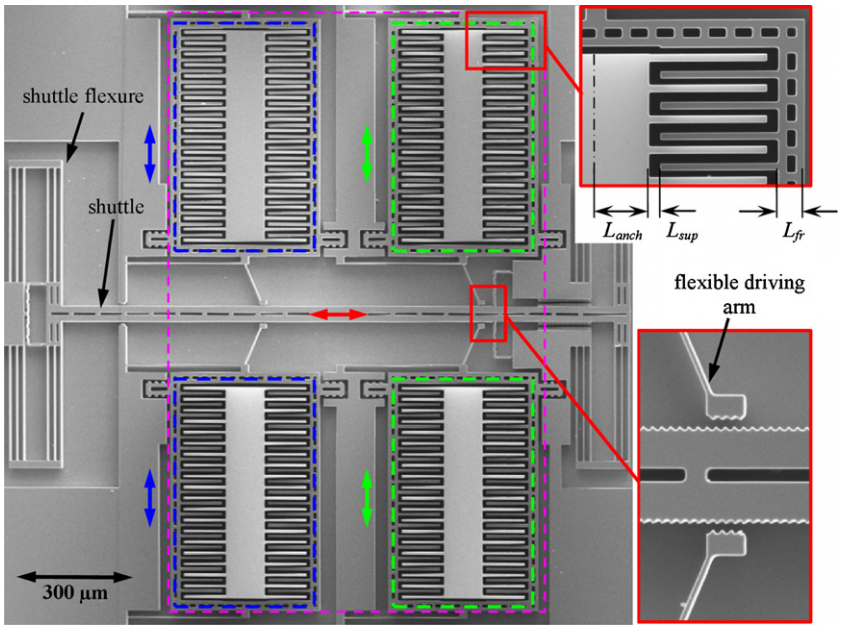

Figure 1. SEM image of the manufactured electrostatic inchworm motor with flexible arm. The dashed lines outline the gap-closing actuators: blue line denotes actuators *A*, green line denotes actuators *B*. The magenta line represents the total area of the motor.

efficiencies. Electrostatic actuators provide average force densities, but they are fast, theoretically have above 90% efficiency [6], and are easy to manufacture and integrate with other microelectromechanical systems (MEMS). While efficiency is high for electrostatic and piezoelectric actuators, they also require high voltages (but negligible currents) for operation, which often results in lower overall efficiency due to the addition of high voltage power electronics. Efficiencies of high voltage amplifiers studied in [1] vary between 30% and 70% with masses below 150 mg. Bellew also showed that high voltages can be provided directly through a MEMS integrable 6.5 mm^2 array of solar cells [7] that generated more than 88 V with a solar efficiency of 14%, which was enough to power a microrobot in [2].

Most microscale actuation methods have force–displacement tradeoffs; high forces can be achieved at the expense of small displacements. Several driving principles have been offered to resolve this issue [8], all of which share the same idea—large displacements are accumulated in stepping (inchworm) motion. For clarity, in the rest of this paper the term 'motor' will refer to the entire driving mechanism (figure 1), and the term 'actuator' will be used to describe a part of the motor—the set of parallel plates that actually generate force when voltage is applied. Inchworm motors can use all three actuation methods described above to create small displacements [9–11]. In this case, electrostatic actuation was chosen over piezoelectric and electrothermal methods. This choice was dictated by its efficiency and straightforward fabrication. For example, the electrostatic actuators fabricated in this paper can be integrated with an SOI (silicon-on-insulator)/elastomer process previously developed by the authors [12] that enables an assembly free manufacturing process of actuated robotic legs or mechanical energy storage mechanisms [13]. A gap-closing configuration [11] of electrostatic actuation was selected over comb drives [14] due to much higher force densities.

Inchworm motion can be accomplished by taking small steps either in-plane or out-of-plane. Out-of-plane inchworm motors are often referred to as shuffle motors due to their shuffling motion across a substrate. These motors can take advantage of small electrostatic gaps or thin beams achievable by depositing thin films during microfabrication whereas in-plane motors are generally limited by lithography. High force density shuffle motors have been presented previously; de Boer demonstrated a shuffle motor with a measured force density of 3.75 $mN\,mm^{-2}$ at 150 V [15] and Sarajlic demonstrated a shuffle motor with a measured force density of 14.3 $mN\,mm^{-2}$ at only 55 V [16].

Despite these impressive numbers, this paper focuses on in-plane electrostatic inchworm motors which require simpler fabrication processes and allow for greater flexibility in mechanism integration. Previous in-plane electrostatic inchworm motors using gap closing actuators have demonstrated relatively poor force densities. Yeh demonstrated a measured force density of 17 $\mu N\,mm^{-2}$ at 33 V (equivalent to 185 $\mu N\,mm^{-2}$ at the 110 V used in this paper) [11]. Erismis demonstrated another electrostatic inchworm motor designed to operate at low voltages with a measured force density of 10 $\mu N\,mm^{-2}$ at 16 V (equivalent to 470 $\mu N\,mm^{-2}$ at 110 V) [17] . In part, these low force densities are due to the use of separate actuators for attaching to the moving shuttle and driving this shuttle forward. Instead, this paper describes a new architecture for in-plane electrostatic inchworm motors that utilize a flexible driving arm (figure 1). As a secondary contribution, this paper develops an optimization process to optimize the entire motor (versus actuators only) for improved force density. Finally, the designed motors were

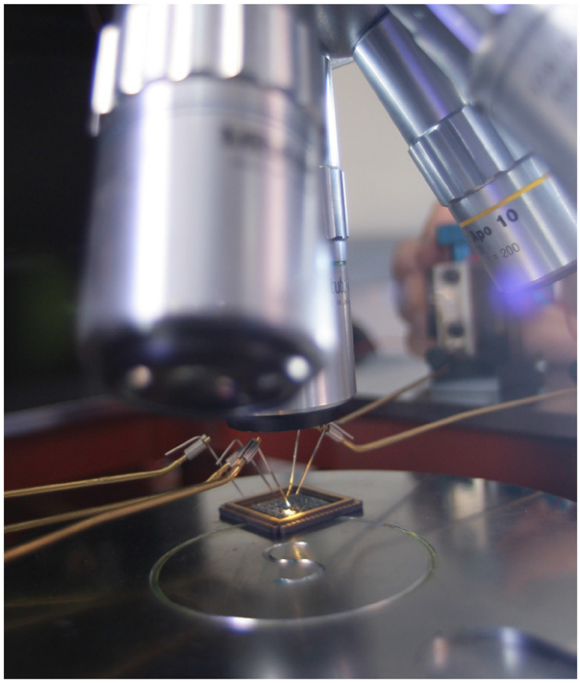

Figure 2. Test setup used to interface with the motors.

fabricated and tested (figure 2) to compare the measured and calculated performances.

This paper is organized as follows. Section 2 describes the principle of operation. The design optimization procedure is outlined in section 3. Section 4 discusses the manufacturing. Finally, section 5 presents experimental test methods and results from manufactured motors.

2. Principle of operation

The idea of inchworm motion is based on accumulating small displacements (steps) to achieve large movements. In-plane inchworm motion is accomplished by using two or more actuators that perform the same cyclic motion in which they engage with a shuttle, move it one step, disengage, and return to the initial position. The actuators operate in anti-phase so that at least one of the actuators is in contact with the shuttle at all times. Several different in-plane inchworm motor designs have been presented previously [2, 8, 10, 11, 17–21]. One disadvantage among previous in-plane designs is the inefficient actuation and use of space which leads to a decrease in force density and efficiency. The inefficiencies are caused either by extra actuators that do not contribute to the output force (e.g. clutch actuators), or by large and unoptimized mechanisms that transfer the driving actuator motion to the shuttle.

The in-plane inchworm motor introduced in this paper implements an angled flexible drive arm that enables both grabbing and pulling the shuttle with one actuator. The symmetric design of the gap-closing actuators on each side of the shuttle balances out the reactions from the engaged drive arms and allows moving even untethered shuttles. This means that the displacements are limited only by the length of the shuttle. The flexible drive arm design offers several advantages over previous designs. First, it substantially

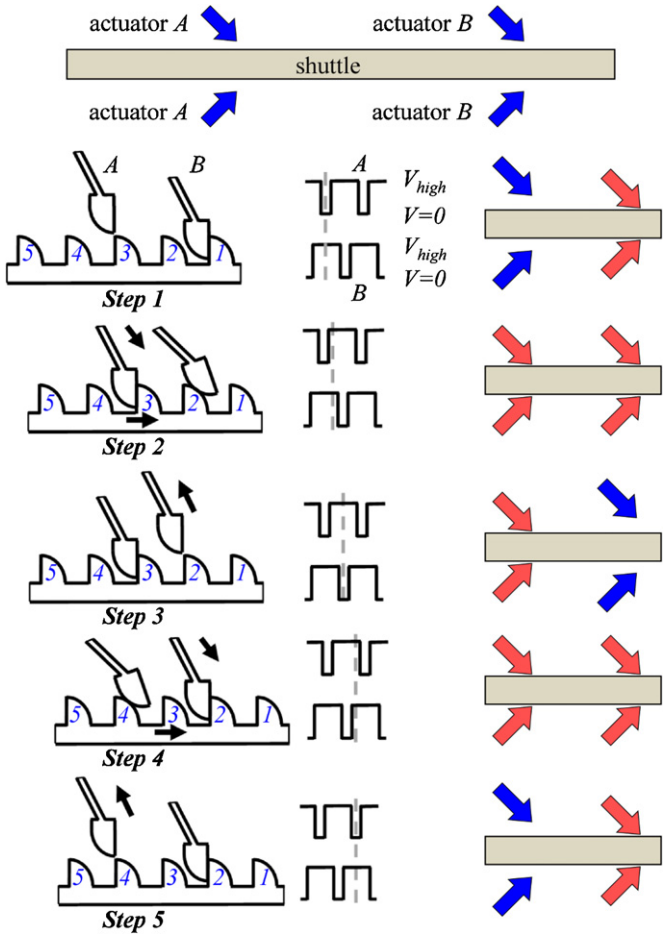

Figure 3. Operation cycle of the inchworm motor with flexible arm. The voltage on each actuator is switched between V_{high} and 0. The voltage is applied on actuators *A* and *B* in anti-phase.

reduces the footprint of the inchworm motor by eliminating the clutch actuator and minimizing the driving mechanism. Second, removal of the clutch actuator simplifies the control of the motor. The new actuator requires only two independent voltage signals (figure 3), unlike previous inchworm motors (table 1). Such a simplification can also be used to increase the motor speed as the time of one step cycle decreases. Finally, removal of the clutch actuators that do not contribute to the motor's output power decreases parasitic capacitance that in turns increases motor efficiency.

As seen in figure 1, the movement of gap-closing actuators (figure 4) is perpendicular to the shuttle; however, the flexible driving arm attached to these actuators is angled with respect to the shuttle. Therefore, upon engagement with the shuttle, the driving arm applies force in both transverse and longitudinal directions. Since the electrostatic actuators on both sides of the shuttle are symmetrical, the transverse forces are equal and opposite in direction, thus their net is zero. The longitudinal forces are equal in magnitude and direction, thus the total pushing force is their sum. Once the electrostatic force overcomes stiffness of the arm and the load force on the shuttle, the arm bends and pushes the shuttle. Thus, movement perpendicular to the actuator displacement is achieved. The operation principle and actuation cycle of the inchworm motor

Table 1. Comparison of inchworm (stepper) motors. Minimum or maximum values in each column are highlighted.

F(mN)	v (mm s^{-1})	A(mm^2)	F/A (mN mm^{-2})	No. C.S.	No. M.S.	V	η (%)	Method*	
0.08	17	0.32	0.25	2	7	9	low	el.th.	[8]
6.7	1	5.25	1.28	2	2	12	10^{-5}	el.th.	[10]
0.06	4	2.8	0.021	4	1	50	–	el.st.	[2]
0.05	4	3	0.017	4	1	33	8	el.st.	[11]
0.11	0.3	10.6	0.010	3	3	16	–	el.st.	[17]
0.45	4.4	0.12	3.75	3	14	150	low	sh.	[15]
1.7	3.6	0.12	14.3	3	4	55	low	sh.	[16]
1.88	**4.8**	**1.36**	**1.38**	**2**	**1**	**110**	**8.8**	el.st.	This work

F—maximum force; v–maximum speed; A—occupied area (estimated from images if not reported); F/A—area force density; C.S.—control signals; M.S.—mask steps; V—applied voltage; η—efficiency.
*el.st.—electrostatic; el.th.—electrothermal; sh.—shuffle.

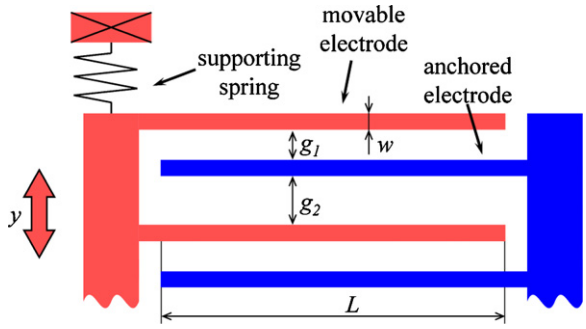

Figure 4. Layout of gap-closing actuator. Blue electrodes are rigidly fixed to an anchor. Red electrodes are supported by a spring and can move in the y direction. w is the width of electrodes, L is the overlapping length of electrodes, g_1 is the forward gap (movement toward the shuttle), g_2 is the backward gap.

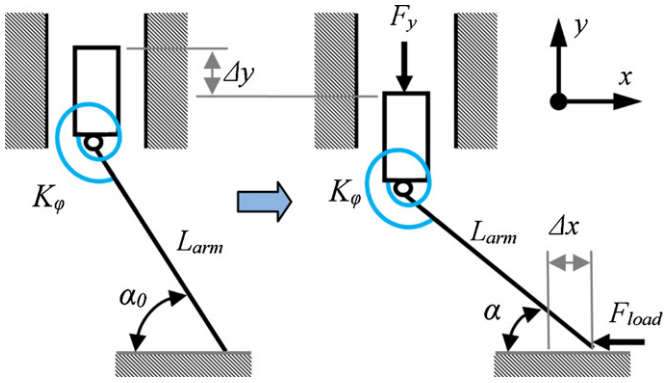

Figure 5. Kinematic diagram of the flexible driving arm where F_y is the force from electrostatic actuator, K_φ is the torsion stiffness of the flexible driving arm, L_{arm} is the length of the arm, Δy is the step displacement of the electrostatic actuator, and Δx is the step displacement of the shuttle.

is represented in figure 3. Initially, one pair of opposite gap-closing actuators engages with the shuttle, pushes it forward and holds it in place. After that, the second pair of actuators engages with the shuttle, pushes it and holds while the first pair is released and returns to its initial position. Repetition of these steps allows for large final displacements. The nature of this design allows driving the shuttle only in one direction. However, if the shuttle is supported by flexures, they will bring it back to its starting location when all actuators are turned off and the arms are disengaged.

3. Design optimization

To decrease the size of the motor while increasing the stall force, it is necessary to optimize the flexible arm mechanism and the layout of the gap-closing actuators. As a direct result of the optimization process, the area force density can be maximized given processing constraints. The optimization procedure is based on the static force equilibrium and procedure described by Yeh [22], in which a similar analysis was performed on an inchworm motor with a combination of clutch and drive gap-closing actuators instead of a flexible arm. This analysis is also extended to optimize the entire motor design instead of focusing solely on the actuators in the motor.

3.1. Mechanism analysis

The main goal of the flexible arm is to transfer force and displacement to the shuttle. To perform these functions, it has to be flexible enough to bend during operation and stiff enough not to buckle. Thus, the flexible driving arm was modeled as a rigid beam with a torsion spring (emulating the arm's bending stiffness) at the pivot point. A kinematic diagram of this mechanism is represented in figure 5. Assuming small movements during one step (Δx, $\Delta y \ll L_{arm}$—length of the driving arm), the displacements of the actuator and shuttle are related as $\Delta x \approx \Delta y \tan\alpha$, where α is the angle of the driving arm in relation to the shuttle. With the same assumptions, the small changes in the arm angle α during a step can be neglected, and the force transferred to the shuttle can be found using static equilibrium conditions. The load force (F_{load}) in figure 5 is

$$F_{load} = \frac{F_y}{\tan\alpha} - K_\varphi \frac{\Delta x}{L_{arm}^2 \sin^2\alpha}, \quad (1)$$

where F_y is the vertical force applied by the electrostatic actuators, and K_φ is the torsion spring constant of the flexible arm. From classical beam theory, K_φ can be estimated as $K_\varphi = EI_{arm}/L_{arm}$, where I_{arm} is the area moment of inertia of the flexible arm's cross section. Since the cross section is a rectangle, $I_{arm} = tb^3/12$, where b and t are the width

and the thickness of the flexible arm, correspondingly. The second term in (1) represents the force that is required to bend the flexible driving arm and can be considered as a loss. To minimize this term, the driving arm has to be very flexible (small K_φ). However, K_φ cannot be too small because the driving arm will be in danger of buckling. Thus, the lower boundary for K_φ (or upper boundary for L_{arm}) is the Euler beam buckling force:

$$F_{\text{buckl}} = \frac{\pi^2 E I_{\text{arm}}}{(K_{\text{b}} L_{\text{arm}})^2} = K_\varphi \frac{\pi^2}{K_{\text{b}}^2 L_{\text{arm}}} > \frac{F_{\text{y}}}{\sin\alpha}, \tag{2}$$

where K_{b} is the beam effective length factor that depends on the conditions of the end support for the beam. In this design, the flexible arm is rigidly fixed to the frame of the gap-closing actuator, but the end that engages with the shuttle can pivot (pin end condition), therefore $K_{\text{b}} = 0.7$. To minimize the losses in the flexible arm, K_φ was set to withhold the applied forces without buckling with a safety factor of n:

$$K_\varphi = \frac{n F_{\text{y}} K_{\text{b}}^2 L_{\text{arm}}}{\pi^2 \sin\alpha} = \frac{E I_{\text{arm}}}{L_{\text{arm}}} \Rightarrow L_{\text{arm}} = \sqrt{\frac{E I_{\text{arm}} \pi^2 \sin\alpha}{n F_{\text{y}} K_{\text{b}}^2}}. \tag{3}$$

Force transferred by the flexible arm is generated by the electrostatic attraction in the gap-closing actuators (figure 4). From [11], this force is

$$F_{\text{el.st.}}(y) = \frac{1}{2}\varepsilon_0 N V^2 L t \left(\frac{1}{(g_1 - y)^2} - \frac{1}{(g_2 + y)^2} \right), \tag{4}$$

where ε_0 is permittivity of free space, N is the number of electrode pairs in the actuator, V is the applied voltage, L is overlapping length of the electrodes, t is the thickness of the electrodes (thickness of the structural layer of the silicon wafer), g_1 and g_2 are the frontside and backside gaps between the electrodes, and y is the actuator displacement. Due to the interdigitated layout of the gap-closing actuator, the movable electrodes experience electrostatic force from both front and back fixed electrodes.

Electrostatic force (4) is not entirely transferred to the shuttle as part of it is spent to deflect the flexures that support the movable set of electrodes (spring constant k_{spr}). Thus, the ultimate force transmitted from actuators to the shuttle through the flexible arm mechanism is

$$F_{\text{y}} = F_{\text{el.st.}} - k_{\text{spr}} \Delta y. \tag{5}$$

For area density calculations, area of the gap-closing actuator (figure 4) is

$$A = N_{\text{act}} N (2w + g_1 + g_2) L, \tag{6}$$

where $N_{\text{act}} = 2$ is the number of actuators in the inchworm motor (A and B in figure 3), and N is the number of electrode pairs in the actuator. This formula accounts only for the area occupied by the electrodes and dismisses the motor periphery, which includes bonding pads, actuator frame, anchors, etc. This simplified area allows for calculating absolute maximum characteristics of the motors, which can be compared to those of other devices. The periphery varies significantly from design to design, and it is difficult to estimate during the initial design stage.

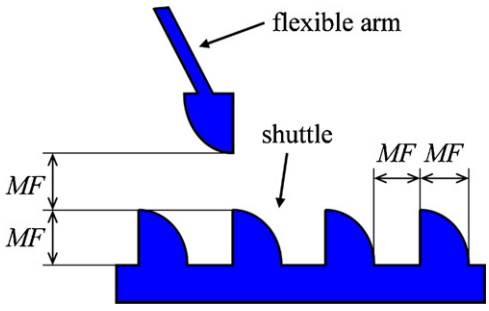

Figure 6. Ratchet teeth between the flexible arm and the shuttle. All teeth are designed to be the size of the minimum feature (MF) size.

3.2. Constraints and limitations

The driving force can be transferred from an actuator to a shuttle through frictional contact [10] or through teeth contact [11]. The main advantage of the frictional contact is the ability to make nanosize steps, which is extremely important for precise positioning applications. The drawbacks of frictional contact are shuttle slipping and the dependence of the step size on the load force [20]. In teeth contact, on the other hand, slipping of the shuttle occurs only at high applied forces, but the step size is limited to the minimal feature (MF) size available from the fabrication process. The teeth layout, shape, and their dimensions are represented in figure 6. For an inchworm mechanism to work, the sum of shuttle displacements from all actuators has to be a multiple of teeth pitch ($2MF$). Since the number of actuators (N_{act}) was chosen to be 2 (A and B), and they are identical, the unit shuttle displacement from one actuator has to be $\Delta x = MF$.

The gaps in the actuator can be calculated based on the ratchet teeth requirements and the arm's angle. The front gap (movement towards the shuttle) consists of three parts. The first part is the distance between the flexible arm and the shuttle; from figure 6 it is equal to $2MF$. The second part is the displacement of the actuator corresponding to movement of the shuttle by one step. From figure 5 this displacement approximately equals to $\Delta y = \Delta x / \tan\alpha$. The last part is the final gap (g_{f}) between electrodes that prevents them from shorting. This gap is necessary due to 'pull-in' instability of the gap-closing actuator [23]. It is realized by introducing mechanical stops that limit the displacement of the movable electrodes. Overall, the front gap of the electrostatic actuator equals to

$$g_1 = 2MF + \Delta y + g_{\text{f}}. \tag{7}$$

The back gap (movement away from the shuttle) has to be larger than the front gap, thus it was assumed that $g_2 = k_{\text{back}} g_1$, where $k_{\text{back}} > 1$. Based on these definitions, when the flexible arm engages with the shuttle, the front and back gaps are

$$\begin{aligned} g_1^{\text{eng}} &= \Delta y + g_{\text{f}} \\ g_2^{\text{eng}} &= k_{\text{back}} g_1 + 2MF. \end{aligned} \tag{8}$$

In this study, k_{back} was set at 1.5. This was done since calculations showed that the backward force is insignificant upon engagement with the shuttle, even with smaller values of k_{back}. However, the dynamics of the gap-closing actuator,

which are not considered in this paper, will prevent the motor from working properly at high speeds if $k_{back} < 1.5$.

Electrostatic force and force density linearly increase with electrode thickness t (4), which is bounded by the limitations of the manufacturing process. Features in the silicon layer are patterned using a deep reactive ion etch (DRIE). The quality of this process is defined by the aspect ratio (depth over width) of the trenches it can etch. Although aspects ratios up to 130 are achievable with the DRIE process [24], in this paper, aspect ratio (λ) was assumed to be 20 as it was limited by the available fabrication tools. The smallest features in the designed motor are the ratchet teeth and the gap between the flexible arm and the shuttle (figure 6). Thus, maximum thickness of the electrodes can be expressed as

$$t = \lambda MF, \; t \leqslant 500 \; \mu\text{m}. \tag{9}$$

The inequality constraint comes from the maximum reasonable thickness of the silicon wafer. It should be noted that due to the single mask manufacturing process, the thickness t of all inchworm motor parts (electrodes, flexures, flexible arm, etc) is assumed to be the same.

Electrostatic force greatly benefits from high actuation voltages since it increases proportionally with V^2 (4). However, 'pull-in' instability of gap-closing actuators imposes constraints on the maximum applied voltage and on the stiffness of the electrode fingers. The final gap g_f prevents shorting only if the electrodes are absolutely rigid (short and thick). Osterberg in [25] derived an expression that relates the maximum voltage and the dimensions of the electrodes, which can be rewritten to define the maximum electrode length for a fixed maximum voltage

$$L_{max} = 4\sqrt{\frac{0.28Ew^3g_f^3}{\varepsilon V^2\left(1+0.42\frac{g_f}{t}\right)}}, \tag{10}$$

where E is the Young's modulus of the electrode's material (silicon).

Gap-closing actuators take advantage of high electric fields (high voltages, narrow gaps) which create the possibility of breakdown of the insulator (air). This issue was investigated extensively in [26] and [27]. The results of studies showed that the breakdown does not occur at voltages below 300 V for any gap. In this paper, all calculations and tests were done at much lower voltage of 110 V.

The set of movable electrodes in the gap-closing actuator is supported by flexures (figure 4). Besides support, the flexures act as spring elements that return electrodes to the initial position when voltages are removed. High stiffness (spring constant) of these flexures reduces the maximum force that the actuator can apply to the shuttle (5). However, the manufacturing process requires the flexures to be robust. Additionally, possible charge entrapment and stiction between the electrodes or friction in the ratchet mechanism require flexures to be reasonably stiff. The maximum spring constant that still allows for pull-in can be calculated as [23]

$$k_{spr}^{max} = \frac{27}{8}\frac{\varepsilon tLN}{g_1^3}V^2. \tag{11}$$

Table 2. Parameters and constants used for optimization procedure.

Parameter	Value/range	Description/justification
MF	$1 \ldots 5$ μm	Based on currently available technologies
α	$10^\circ \ldots 85^\circ$	Entire range, except extremes
g_f	1 μm	Final gap, based on previous testing experience
N	40	Number of pairs of electrodes in each actuator
V	110 V	Maximum applied voltage, based on previous testing experience
λ	20	DRIE aspect ratio, based on available equipment characteristics
n	2	Safety factor for flexible arm buckling constraint (2)
K_b	0.7	Beam effective length factor in (2)
E	170×10^9 Pa	Averaged Young's modulus of silicon

3.3. Force density optimization

In this paper, the force density is defined as the ratio of the actuator force transferred to the shuttle (F_{load}) to the area occupied by the electrodes (A). The constant parameters used in the study are shown in table 2. The spring constant of the actuator flexures was calculated to maintain the resonant frequency of the actuator at 10 kHz. This number was chosen based on preliminary tests; higher frequencies are infeasible in this modeling due to unaccounted viscous damping, which becomes dominant as operating frequencies increase. The resonant frequency was calculated as

$$f_{res} = \frac{1}{2\pi}\sqrt{\frac{k_{spr}}{m}} = \frac{1}{2\pi}\sqrt{\frac{k_{spr}}{\rho tLwN}}, \tag{12}$$

where ρ is the density of silicon. The optimization problem is defined as

$$\begin{aligned} \underset{MF,\alpha,w}{\text{maximize}} \quad & F_{load}/A \\ \text{subject to} \quad & g_1 = 2MF + \Delta y + g_f \\ & g_2 = k_{back}g_1 \\ & t = \lambda MF \leqslant 500 \; \mu\text{m} \\ & L \leqslant L_{max} \\ & k_{spr} \leqslant k_{spr}^{max} \\ & f_{res} = 10 \text{ kHz}. \end{aligned} \tag{13}$$

The optimization was performed in MATLAB. A regular 2D mesh in the MF-α plane was generated, and the MATLAB native function `fmincon` was used to compute the maximum of the objective function (F_{load}/A) at the mesh points with the aforementioned constraints.

The calculated force density as a function of minimum feature and flexible arm angle is shown in figure 7. The bold red line traces maximum of force density for different values of MF. The blue star marks the maximum force density for given constraints which was calculated to be 10.9 mN mm^{-2} at $MF = 1$ μm, $\alpha = 55^\circ$, and $w = 1$ μm.

Several conclusions can be drawn from the results of the optimization. Firstly, the objective function increases as minimum feature size decreases, even though the thickness of inchworm motor components changes linearly with MF (9). This happens since smaller values of MF simultaneously

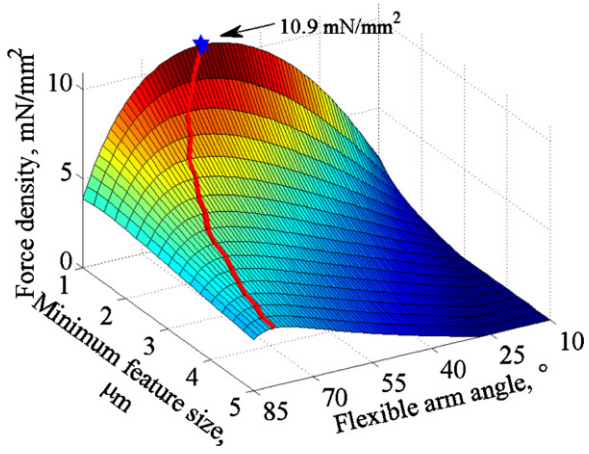

Figure 7. Theoretical force density of the new inchworm motor (at 110 V). The blue star indicates the maximum of force density ($MF = 1\ \mu$m, $\alpha = 55^\circ$).

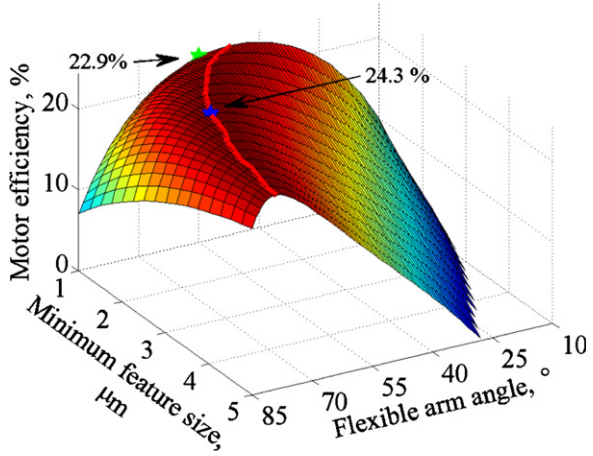

Figure 8. Motor efficiency in the force density optimization. The blue star indicates the maximum motor efficiency ($MF = 2.75\ \mu$m, $\alpha = 71^\circ$). The green star indicates the motor efficiency at the maximum of force density ($MF = 1\ \mu$m, $\alpha = 55^\circ$).

increase the numerator (F_{load}) and decrease the denominator (A) of the objective function. Secondly, the maximum of the objective function is achieved at the lowest boundary of the electrode width w. It can be shown that for the given constraints the force density changes as $1/w$.

3.4. Motor efficiency

Maximum theoretical efficiency of an electrostatic gap-closing actuator can be calculated by making a few simple assumptions. Firstly, it is assumed that the total energy transferred to the actuator from a power supply is equal to the maximum energy stored in the capacitor formed by the interdigitated electrodes. Maximum energy implies that it is calculated for the largest possible capacitance which is achieved when the gap between the electrodes is the smallest possible. Then, the total energy input equals

$$E = \frac{1}{2}CV^2 = \frac{1}{2}\frac{\varepsilon NtL}{g_{\text{f}}}V^2. \tag{14}$$

Secondly, it is assumed that the actuator works against a constant load for each step. This is a valid assumption because the displacement of the actuator is small. The work performed by the actuator can be calculated as

$$W = F_{\text{eng}}\Delta y = \frac{1}{2}\frac{\varepsilon NtL}{g_{\text{eng}}^2}V^2\Delta y, \tag{15}$$

where F_{eng} and g_{eng} are the actuator force and gap between electrodes at the moment the angled arm engages with the shuttle. Even though actuator force will increase as the shuttle is pushed forward, it is assumed that useful work on a load is limited to this initial engagement force. Efficiency of the actuator is defined as the ratio of work done to the transferred energy

$$\eta = \frac{W}{E} = \frac{g_{\text{f}}\Delta y}{g_{\text{eng}}^2}, \tag{16}$$

but $\Delta y = g_{\text{eng}} - g_{\text{f}}$, then (16) becomes

$$\eta = \frac{g_{\text{f}}(g_{\text{eng}} - g_{\text{f}})}{g_{\text{eng}}^2} = \frac{g_{\text{f}}g_{\text{eng}} - g_{\text{f}}^2}{g_{\text{eng}}^2} = s - s^2,$$

where $s = g_{\text{f}}/g_{\text{eng}} < 1$. Simple calculation shows that the maximum of this expression is achieved at $s = 0.5$ and equals to $\eta = 0.25$ or 25% for an inchworm gap-closing actuator that is voltage driven. This limit is much smaller than the theoretical efficiency for electrostatic actuators (90%) in general due to the limitations of the chosen mechanism and the constraints of the manufacturing process.

The designed inchworm motor contains four gap-closing actuators, thus its overall efficiency cannot exceed individual efficiency of the actuators. In fact, efficiency in a full inchworm motor with a flexible arm is less than 25% due to losses in the flexible arm and flexures. By accounting for these force losses, the inchworm motor efficiency was calculated in the force density optimization analysis. The maximum calculated efficiency of 24.3% was achieved at $MF = 2.75\ \mu$m, $\alpha = 71^\circ$ (figure 8). Although locations of the efficiency maximum and force density maximum were different, the efficiency values at these two points varied only by 1.4%.

3.5. Optimization for a full motor design

The force density optimization above was done without accounting for peripheral structures in the actuators. This is useful for obtaining absolute characteristics for comparison with other types of motors. However, in designing the motor with a specific layout in mind, the periphery, such as the electrode anchors, the rigid frame and the area occupied by the flexible arms, has to be accounted for. Figure 9 represents a force density optimization done for a design with 100 μm-wide anchors, 10 μm wide electrode support, 25 μm wide frames, and the maximum thickness of 40 μm for the inchworm motor components. These parameters were chosen based on previous design experience and wafer availability. Also, the total area in this model accounts for the area occupied by the flexible arms

$$A_{\text{n}} = N_{\text{act}}[(N(2w + g_1 + g_2)) + L_{\text{arm}}\sin(\alpha)] \times (L + L_{\text{sup}} + L_{\text{fr}} + L_{\text{anch}}), \tag{17}$$

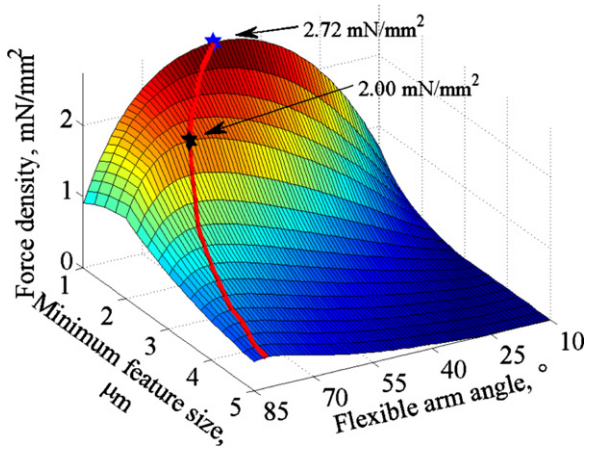

Figure 9. Theoretical force density of the inchworm motor with designed periphery (at 110 V). The blue star indicates the maximum of force density ($MF = 1$ μm, $\alpha = 52°$). The black star indicates the maximum of force density for the smallest MF size available for manufacturing ($MF = 2$ μm, $\alpha = 69°$).

Table 3. Calculated characteristics of the manufactured motors.

MF	α	w	L	L_{arm}
2 μm	69°	7.28 μm	104 μm	124 μm
g_1	g_2	t	k_{spr}	$F_{load/A}$
5.77 μm	8.65 μm	40 μm	11.1 μN μm^{-1}	2.00 mN mm^{-2}

where $L_{fr} = 10$ μm is the frame width, $L_{anch} = 50$ μm is the anchor half-width, $L_{sup} = 10$ μm is the electrode support (figure 1), and L_{arm} is the length of the flexible arm .

The blue star in figure 9 marks the maximum force density for given constraints which was calculated to be 2.72 mN mm^{-2} at $MF = 1$ μm, $t = 20$ μm, $\alpha = 52°$, $w = 5.09$ μm, and calculated efficiency with this design of 23.0%. However, the available processing tools allowed fabrication only with 2 μm minimum feature size. Thus, the inchworm motors were designed for $MF = 2$ μm and $\alpha = 69°$ (black star in figure 9). All calculated characteristics and dimensions for this motor design are represented in table 3.

It should be noted that one of the effects of accounting for periphery is a change in the optimal values of the optimization analysis. In section 3.3, the electrode width was equal to the minimum feature size (lower boundary of w). Inclusion of the periphery in the analysis shifted w away from the lower boundary. The optimal value of electrode length L changed as well according to (10). Therefore, it is very important to account for all periphery of the inchworm motors when designing for manufacturing.

The results of the optimization demonstrate that manufacturing limitations (minimum feature size and aspect ratio) are the main obstacles toward creating in-plane electrostatic inchworm motors with force densities exceeding shuffle or electrothermal motors. By increasing the aspect ratio (λ) five times to 100 : 1, the maximum motor force density will be 13.7 mN mm^{-2} —almost as high as in the shuffle motors (table 1). Also, a high aspect ratio allows using thicker wafers without sacrificing the minimum feature size which will improve robustness of the inchworm motors and will encourage their integration into more systems.

4. Fabrication

The inchworm motors were fabricated on a SOI wafer (40 μm structural layer, 5 μm oxide layer) using a standard SOI manufacturing process. The devices were transferred to the silicon layer in a single DRIE step with 2 μm minimum feature size. After the etch, the wafer was coated with photoresist to protect small gaps from particle contamination and diced. Then, the photoresist layer was ashed with oxygen plasma and devices were released by wet etching the buried oxide in 49% hydrofluoric (HF) acid. No stiction of silicon features was observed during drying of devices due to thick structural and oxide layers. After drying, aluminum wires were bonded directly to the silicon pads. To prevent electrical shorting of the electrodes in accidental contact during the tests, a 150 nm layer of aluminum oxide (Al_2O_3) was conformally deposited on the released structures using an atomic layer deposition process [28]. Also, Mayer showed that Al_2O_3 layer decreases friction and is a good wear resistive coating [29] which is important for ratchet teeth operation. Overall, fabrication showed a high yield (>90%), where the largest source of defects was the photolithography step.

The tests of the manufactured motors showed that the mechanism as designed is insensitive to the final shape of the ratchet teeth which are often significantly affected by fabrication. Figure 10 demonstrates a comparison of the designed layout of the ratchet teeth and their shape in two fabricated devices (on different wafers and different MF size). The variations of shape in manufactured teeth are a result of different parameters during the DRIE step and smaller teeth size. Despite such drastic variations in teeth shape, both ratchet mechanisms performed properly and pushed the shuttle without slipping.

5. Results

The optimization analysis above provided the basis for design and manufacture of the electrostatic inchworm motor. Dimensions of manufactured devices were chosen from the results of the force density optimization with periphery (section 3.5). The design was selected for the highest force density at $MF = 2$ μm, which was the smallest feature size available for fabrication. The dimensions and the calculated characteristics are listed in table 3. The motors were actuated using a square wave signal (figure 3) with a maximum voltage of 110 V. The maximum voltage was determined based on preliminary tests of electrostatic actuators. At this voltage level the actuators showed repeatable performance, whereas at higher voltages charge entrapment in the deposited aluminum oxide caused opposite electrodes to stick even when the voltage was turned off. Tests showed that the layer of Al_2O_3 increased the pull-in voltage only by several volts. Considering that actuation was done with 110 V, this influence was neglected in the modeling. The larger effect charge entrapment had on the voltage level at which the actuators disengaged. This voltage, however, is not part of the model, thus this effect was not taken into account.

The stiction of actuators during operation decreased dramatically in motors with Al_2O_3 due to the frequent contact

Table 4. Comparison of analytical and measured characteristics of the supporting flexures.

Flexure	Spring constant (N m^{-1})		Ratio	Resonant frequency (kHz)		Ratio^2
length (μm)	Analytical	Measured	(an./m.)	Analytical	Measured	(an./m.)^2
300	40.8	19.8	2.06	10.7	7.43	2.07
350	25.7	12.6	2.04	8.48	5.94	2.04
400	17.2	8.60	2.0	6.94	4.85	2.05

and welding of the fingers in the uncoated devices. The long term tests showed that after approximately 1 million engagements of the flexible arm and the shuttle, some debris started accumulating between the teeth and while the motor still worked, performance became unpredictable.

5.1. Calibration

Direct force measurement in MEMS actuators is a difficult task due to the small actuator size and the lack of suitable sensors. The more common indirect measurement method calculates the force from the deflection of a spring mechanism (shuttle flexure) that is moved by the motor. Then, assuming that deformations are linear, the motor force is

$$F = k_{\text{flex}} \cdot \Delta x, \tag{18}$$

where k_{flex} is the spring constant of shuttle flexures, and Δx is its displacement.

In this research displacement measurements were done using an optical microscope by monitoring movement of a regular pattern on the object of interest [30]. Spring constants were measured using simplified analysis techniques proposed by Clark [31]. Several comb drive resonators with three types of flexures were placed on each die. These flexures were identical in design to the ones supporting the shuttle in the inchworm motors but with varying length and, therefore, spring constant. The obtained calibrated flexure spring constants were used in the later sections for performance characterization of the manufactured inchworm motors. The measured data and its comparison with analytical values is shown in table 4. Analytical values were based on the designed dimensions accounting for the lateral etch from SEM measurements. The same dimensions were used to calculate the analytical resonant frequency from (12). The measurements of resonant frequency were performed by actuating the comb drives with a biased sinusoidal signal and visually observing the amplitude of vibrations.

The calibrated spring constants were approximately a half of the analytically predicted values. Reasons for such a dramatic difference include fluctuations in lateral etch, the footing effect in DRIE on SOI wafers, and imprecise values of the material properties. More detailed inspection of the manufactured features showed gradual widening of the DRIE trenches closer to the bottom which resulted in trapezoidal cross section of silicon features. Considering that bending stiffness of flexures varies with width cubed, even small change in lateral dimensions will result in significant change of spring constant.

The measured resonant frequency showed the same deviation from the analytical values as the capacitance measurements. Although the performed frequency measurements are more straightforward than the capacitance measurements, generally they do not provide the same level of accuracy since the resonant mass can only be estimated based on the known dimensions. However, the resonant frequency can be used to estimate the damping effects or the change in the resonant mass.

5.2. Maximum load

Maximum load is the maximum force on the shuttle that can be held by the flexible arm mechanism. Due to the intentional flexibility of the driving arms, the major concern before testing was buckling or breaking of the arms at high loads. The testing, however, showed that the primary failure mechanism was not buckling during operation of the motor but snapping of the flexible arms during the release of the shuttle after the test. This failure was occasional and happened only for loads greater than 1.5 mN.

The measurements of the maximum load were done by applying voltage to one set of electrostatic actuators so that the flexible arms engaged with the shuttle and held it in place. Then, the shuttle was manually pushed with a probe in the direction that the motor pushes it. This was done until upon removing of the probe, the restoring force from the flexures

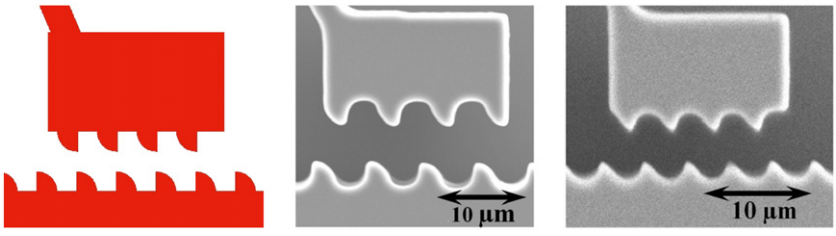

(*a*) (*b*) (*c*)

Figure 10. Teeth shape comparison. (*a*) Layout of ratchet teeth. (*b*) Manufactured teeth with 3 μm minimum feature (and teeth) size. (*c*) Manufactured teeth with 2 μm minimum feature (and teeth) size.

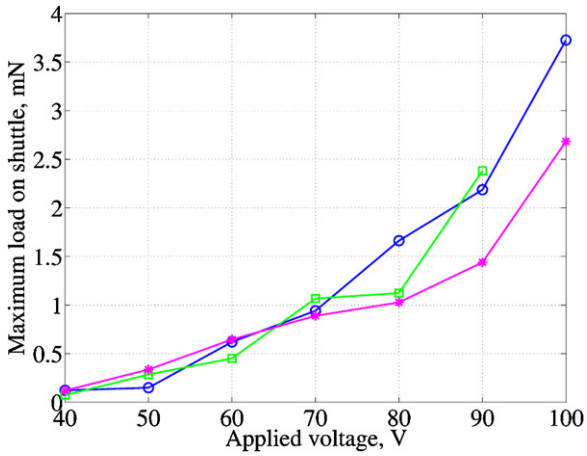

Figure 11. Plots of maximum load as a function of voltage.

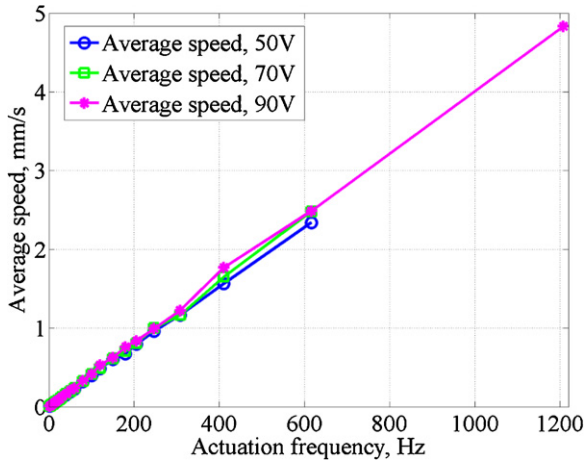

Figure 12. Plot of average shuttle speed at different driving frequencies and voltages.

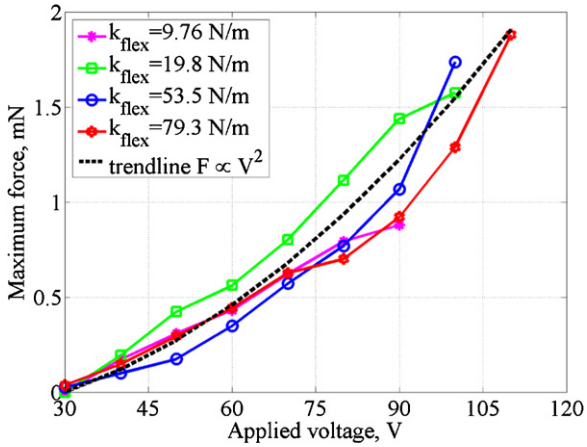

Figure 13. Measured maximum shuttle force as a function of applied voltage. Black dashed line is a trendline demonstrating proportionality of the maximum force to V^2.

became strong enough to force the shuttle to slip against the teeth contact. The results of the tests on three different motors are presented in figure 11. During these tests, none of the flexible arms were broken or buckled. The slipping of the shuttle occurred when the load overcame the actuator force and pushed the engaged electrodes apart. Due to the dependence of the electrostatic force on the gap between the electrodes (4), as soon as the gap increases, the slipping process becomes uncontrollable. The plots in figure 11 demonstrate that the maximum load strongly depends on the actuating voltage. These measurements were limited by the maximum displacement of the shuttle, thus only loads below 3.7 mN could be tested.

The results of this test show that although the flexible arms are capable of withstanding at least 3.7 mN of static load, snapping failure occurs at lower loads. We hypothesize that this problem can be alleviated by increasing the stiffness of the actuator flexures so that flexible arms disengage the shuttle faster upon release. This hypothesis will be verified in the future works.

5.3. Maximum speed

Maximum speed of the shuttle is a function of the driving voltage frequency. The maximum speed can be achieved if the gap-closing actuators are driven at resonance. This, however, is not a straightforward procedure, as the gap-closing actuators tend to move in a backward direction at the high driving frequencies (dynamic 'pull-in' [32]). This happens due to the nature of electrostatic force and design of the gap-closing actuator. The moving electrodes in a gap-closing actuator are moving towards the closer fixed electrode. At low frequency actuation, the dynamic effects can be neglected; however, at high frequency actuation, the back electrode can be closer than the front if the system is underdamped. Thus, when voltage is applied, the actuator can move backwards, which will result in disruption of the inchworm cycles and slipping of the shuttle.

Figure 12 illustrates the dependence of the shuttle velocity on driving frequency. As expected, this dependence is linear due to constant step sizes, and does not vary for different driving voltages. The shuttle velocity was calculated as follows: the motor was driven for 15 cycles, then the total displacement of the shuttle was measured and divided by the total time required for 15 cycles. All of these tests were done at loads less than the maximum (section 5.2) thus no shuttle slipping was observed. The maximum repeatable speed was achieved at 1.2 kHz actuation frequency, which corresponds to a shuttle velocity of 4.8 mm s^{-1}. The maximum speed was repeatedly observed only at 90 V and higher voltages.

5.4. Maximum force

The maximum force (stall force) that the actuators can transfer to the shuttle was measured based on the calibrated flexure stiffness. The motor was actuated until the shuttle stopped moving. Then, the total shuttle displacement was measured from a micrograph, and the stall force was calculated from (18). The results of tests with different flexures are represented in figure 13.

The maximum observed displacement was 124 μm in the test with the 'softest' flexure (9.76 N m^{-1}) at 110 V. A maximum force of 2.23 mN at 120 V was achieved in the test

with the 'stiffest' flexure (79.3 $\mathrm{N\,m^{-1}}$); however, to remain consistent with the optimization analysis the maximum value at 110 V (1.88 mN) will be considered in further analysis. This maximum force at 110 V is just 10.5% smaller than the one calculated in the optimization analysis (2.10 mN), which demonstrates the reliability of the model. The area occupied by the motor is 1.36 $\mathrm{mm^2}$ (including all of the peripheral structures), resulting in a realized force density of 1.38 $\mathrm{mN\,mm^{-2}}$. This measured force density is considerably less than the expected optimized value of 2.00 $\mathrm{mN\,mm^{-2}}$. The primary reason for this is an underestimation of the required periphery by the model. The additional periphery is required for easier motor testing and can be significantly decreased for motors designed with specific applications in mind.

The maximum force of the motor shows a quadratic dependence on voltage, as expected for the motor using gap-closing actuators (4). The trendline in figure 13 ($F = 0.17(V^2 - V_{\mathrm{pull-in}}^2)$) demonstrates this proportionality. Zero of the actuator force is shifted due to counteraction of the actuator's supporting flexures.

5.5. Motor efficiency

The motor efficiency was calculated as the maximum useful work that the motor can perform divided by the total energy stored in the capacitor formed by the gap closing electrodes. The maximum work is achieved at maximum force since the step size is constant. Thus, $W_{\mathrm{max}} = F_{\mathrm{max}}\Delta x$, where $F_{\mathrm{max}} = 1.88$ mN at 110 V (from section 5.4) and $\Delta x = 2\ \mu$m was measured in shuttle force tests. The maximum energy stored in the gap-closing actuator can be calculated from $E = \frac{1}{2}CV^2$, and its maximum is achieved when the capacitance is the largest and the front gap is the smallest. Capacitance measurements showed that the capacitance of the gap-closing actuators when first engaging with the shuttle was 5.60 pF and increased to 7.10 pF when fully actuated to the final gap, which includes any parasitic capacitance due to packaging and wiring. Therefore, the manufactured motor efficiency is $\eta_{\mathrm{calc}} = W_{\mathrm{max}}/E_{\mathrm{max}} = 8.75\%$.

6. Conclusions and future work

A new motor architecture to improve force density and efficiency in in-plane electrostatic inchworm motors has been introduced and an optimized design has been fabricated and tested. Although some of the shuffle and electrothermal motors demonstrate better force parameters, they lack in efficiency or require complex manufacturing process. The primary innovation in this design is the use of a flexible driving arm mechanism to accumulate small displacements from arrays of gap closing actuators to a motor shuttle. An optimization process, developed based on an analytical model for this new motor design, showed that taking the motor support structures into account can influence not only force density, but optimal design variables as well. For example, in the optimization with minimum feature size of 2 μm, an etch aspect ratio of 20 : 1, and 110 V the maximum force density and optimal electrode width change from 6.95 $\mathrm{mN\,mm^{-2}}$ and 2 μm to 2.00 $\mathrm{mN\,mm^{-2}}$ and 7.28 μm, respectively, when support structures are taken into account.

The inchworm motor optimized for the maximum force density was fabricated in a single mask SOI process and evaluated using calibrated springs for a more accurate measure of force output. The motor demonstrated robust performance, speeds up to 4.8 $\mathrm{mm\,s^{-1}}$, and a maximum shuttle force of 1.88 mN at 110 V. This measured force was within 10% of the force predicted by the analytical model during the optimization. The resulting force density of 1.38 $\mathrm{mN\,mm^{-2}}$ is several times higher than demonstrated by previous in-plane electrostatic inchworm motors (table 1), many of which likely overestimate force due to lack of calibration in force measurements. Finally, using capacitance-based measurement methods, the measured efficiency of the inchworm motor was 8.75%—much lower than the model predicted value of 23.6%, primarily due to not accounting for the parasitic capacitance of the wiring and motor packaging in the model.

Future work will include redesign and fabrication of motors with better manufacturing tools and tighter requirements on the periphery. This will further improve force density and efficiency. Also, alternative ways of powering the motors will be studied, such as pseudo-adiabatic charging, to improve energy transfer efficiency to the actuators up to 90% [33]. Finally, motor speed and power can be further improved through studying the motor dynamics and optimizing based on these results.

Acknowledgments

This work was supported in part by the National Science Foundation under Award ECCS1055675. In addition, we acknowledge the support of the Maryland NanoCenter and its FabLab. Also, the authors are grateful to Dr Andrew Harris for the permission to use his lab equipment.

References

[1] Karpelson M, Wei G Y and Wood R J 2008 A review of actuation and power electronics options for flapping-wing robotic insects *IEEE Int. Conf. on Robotics and Automation* pp 779–86

[2] Hollar S, Flynn A, Bergbreiter S and Pister K S J 2005 Robot leg motion in a planarized-SOI, two-layer poly-si process *J. Microelectromech. Syst.* **14** 725–40

[3] Dechev N, Cleghorn W L and Mills J K 2004 Microassembly of 3D microstructures using compliant, passive microgripper *J. Microelectromech. Syst.* **13** 176–89

[4] Ebefors T, Mattsson J U, Kalvesten E and Stemme G 1999 A walking silicon micro-robot *10th Int. Conf. on Solid State Sensors and Actuators (Japan)* pp 1202–5

[5] Sreetharan P S, Whitney J P, Strauss M D and Wood R J 2012 Monolithic fabrication of millimeter-scale machines *J. Micromech. Microeng.* **22** 055027

[6] Bell D J, Lu T J, Fleck N A and Spearing S M 2005 MEMS actuators and sensors: observations on their performance and selection for purpose *J. Micromech. Microeng.* **15** S153–64

[7] Bellew C L, Hollar S and Pister K S J 2003 An SOI process for fabrication of solar cells, transistors and electrostatic actuators *12th Int. Conf. on Solid-State Sensors, Actuators and Microsystems* vol 2 pp 1075–8

[8] Arthur C, Ellerington N, Hubbard T and Kujath M 2011 MEMS earthworm: a thermally actuated peristaltic linear micromotor *J. Micromech. Microeng.* **21** 035022
[9] Toda R and Yang E H 2007 A normally latched, large-stroke, inchworm microactuator *J. Micromech. Microeng.* **17** 1715–20
[10] Maloney J M, Schreiber D S and DeVoe D L 2004 Large-force electrothermal linear micromotors *J. Micromech. Microeng.* **14** 226–34
[11] Yeh R, Hollar S and Pister K S J 2002 Single mask, large force and large displacement electrostatic linear inchworm motors *J. Microelectromech. Syst.* **11** 330–6
[12] Gerratt A P, Penskiy I and Bergbreiter S 2010 SOI/elastomer process for energy storage and rapid release *J. Micromech. Microeng.* **20** 104011
[13] Gerratt A P, Penskiy I and Bergbreiter S 2010 Integrated silicon-PDMS process for microrobot mechanisms *IEEE Int. Conf. on Robotics and Automation* pp 3153–8
[14] Tang W C, Lim M G and Howe R T 1992 Electrostatic comb drive levitation and control method *J. Microelectromech. Syst.* **1** 170–8
[15] deBoer M P, Luck D L, Ashurst W R, Maboudian R, Corwin A D, Walraven J A and Redmond J M 2004 High-performance surface-micromachined inchworm actuator *J. Microelectromech. Syst.* **13** 63–74
[16] Sarajlic E, Yamahata C, Berenschot E, Tas N, Fujita H and Krijnen G 2010 High-performance shuffle motor fabricated by vertical trench isolation technology *Micromachines* **1** 48–67
[17] Erismis M A, Neves H P, Puers R and Van Hoof C 2008 A low-voltage large-displacement large-force inchworm actuator *J. Microelectromech. Syst.* **17** 1294–301
[18] Daneman M J, Tien N C, Solgaard O, Pisano A P, Lau K Y and Muller R S 1996 Linear microvibromotor for positioning optical components *J. Microelectromech. Syst.* **5** 159–65
[19] Kim S H, Hwang I H, Jo K W, Yoon E S and Lee J H 2005 High-resolution inchworm linear motor based on electrostatic twisting microactuators *J. Micromech. Microeng.* **15** 1674–82
[20] Tas N R, Sonnenberg T, Molenaar R and Elwenspoek M 2003 Design, fabrication and testing of laterally driven electrostatic motors employing walking motion and mechanical leverage *J. Micromech. Microeng.* **13** N6–15
[21] Baltzer M, Kraus T and Obermeier E 1997 A linear stepping actuator in surface micromachining technology for low voltages and large displacements *Int. Conf. on Solid State Sensors and Actuators* vol 2 pp 781–4
[22] Yeh R 2001 Articulated mechanisms and electrostatic actuators for autonomous microrobots *PhD Thesis* University of California, Berkeley
[23] Hung E S and Senturia S D 1999 Extending the travel range of analog-tuned electrostatic actuators *J. Microelectromech. Syst.* **8** 497–505
[24] Rangelow I W 2003 Critical tasks in high aspect ratio silicon dry etching for microelectromechanical systems *J. Vac. Sci. Technol.* A **21** 1550–62
[25] Osterberg P M and Senturia S D 2002 M-TEST: a test chip for MEMS material property measurement using electrostatically actuated test structures *J. Microelectromech. Syst.* **6** 107–18
[26] Chen C H, Yeh J A and Wang P J 2006 Electrical breakdown phenomena for devices with micron separations *J. Micromech. Microeng.* **16** 1366–73
[27] Ono T, Sim D Y and Esashi M 2000 Micro-discharge and electric breakdown in a micro-gap *J. Micromech. Microeng.* **10** 445–51
[28] Hoivik N D, Elam J W, Linderman R J, Bright V M, George S M and Lee Y C 2003 Atomic layer deposited protective coatings for micro-electromechanical systems *Sensors Actuators* A **103** 100–8
[29] Mayer T M, Elam J W, George S M, Kotula P G and Goeke R S 2003 Atomic-layer deposition of wear-resistant coatings for microelectromechanical devices *Appl. Phys. Lett.* **82** 2883
[30] Yamahata C, Sarajlic E, Krijnen G J M and Gijs M A M 2010 Subnanometer translation of microelectromechanical systems measured by discrete fourier analysis of CCD images *J. Microelectromech. Syst.* **19** 1273–5
[31] Clark J V, Garmire D, Last M, Demmel J and Govindjee S 2004 Practical techniques for measuring MEMS properties *NSTI-Nanotech Conf. (Boston, MA, USA)* vol 1, pp 402–5
[32] Alsaleem F M, Younis M I and Ouakad H M 2009 On the nonlinear resonances and dynamic pull-in of electrostatically actuated resonators *J. Micromech. Microeng.* **19** 045013
[33] Paul S, Schlaffer A M and Nossek J A 2000 Optimal charging of capacitors *IEEE Trans. Circuits Syst. I* **47** 1009–16